RESEARCH ARTICLE | NOVEMBER 14 2024

Mn_3Sn-based noncollinear antiferromagnetic tunnel junctions with bilayer boron nitride tunnel barriers

Zhanran Wang ; Bo Bian ; Lei Zhang ; Zhizhou Yu

Appl. Phys. Lett. 125, 202404 (2024)
https://doi.org/10.1063/5.0234130

Mn_3Sn-based noncollinear antiferromagnetic tunnel junctions with bilayer boron nitride tunnel barriers

Cite as: Appl. Phys. Lett. **125**, 202404 (2024); doi: 10.1063/5.0234130
Submitted: 20 August 2024 · Accepted: 7 November 2024 ·
Published Online: 14 November 2024

Zhanran Wang,[1] Bo Bian,[1] Lei Zhang,[2,a)] and Zhizhou Yu[1,a)]

AFFILIATIONS

[1]Center for Quantum Transport and Thermal Energy Science, Institute of Physics Frontiers and Interdisciplinary Sciences, School of Physics and Technology, Nanjing Normal University, Nanjing 210023, China
[2]State Key Laboratory of Quantum Optics and Quantum Optics Devices, Institute of Laser Spectroscopy, Shanxi University, Taiyuan 030006, China

[a)]Authors to whom correspondence should be addressed: zhanglei@sxu.edu.cn and yuzhizhou@njnu.edu.cn

ABSTRACT

Electrical manipulation and detection of antiferromagnetic states have opened a new era in the field of spintronics. Here, we propose a noncollinear antiferromagnetic tunnel junction (AFMTJ) consisting of noncollinear antiferromagnetic Mn_3Sn as electrodes and a bilayer boron nitride as the insulating layer. By employing the first-principles method and the nonequilibrium Green's function, we predict that the tunneling magnetoresistance (TMR) of the AFMTJ with AA- and AB-stacked boron nitride can achieve approximately 97% and 49%, respectively. Moreover, different orientations of the Néel vector in the electrodes lead to four distinct tunneling states in the Mn_3Sn/bilayer BN/Mn_3Sn AFMTJ. The TMR ratio could be notably improved by adjusting the chemical potentials, reaching up to approximately 135% at a chemical potential of 0.1 eV for the AFMTJ with AA-stacked boron nitride. This enhancement can be primarily attributed to the reduction in the transmission of antiparallel configurations around the K and K' points in the two-dimensional Brillouin zone. Our findings could provide extensive opportunities for all-electrical reading and writing of the Néel vector of noncollinear antiferromagnets, paving the way for the development of antiferromagnetic tunnel junctions with two-dimensional tunnel barriers.

Antiferromagnets have attracted significant interest in the next generation of spintronics for potential applications in high-density and ultrafast memory devices due to their unique advantages over ferromagnets, such as insensitivity to magnetic perturbations, the absence of stray fields, and ultrafast dynamics.[1–7] Due to the zero net magnetization, the Néel vector of antiferromagnets is difficult to control by external magnetic fields. Therefore, manipulating and detecting the Néel vector by electric means has received intense attention. It has been demonstrated that the Néel vector of antiferromagnets can be effectively manipulated by utilizing the current-induced spin–orbit torque induced by the Edelstein effect.[8–11] Moreover, the detection of the Néel vector has been realized by using anisotropic magnetoresistance[12] and spin Hall magnetoresistance effects.[13–15] However, the electric signals detected by both methods are relatively small and thereby could be easily influenced,[16] hindering the practical applications of antiferromagnetic (AFM) spintronic devices. Recently, Shao *et al.* proposed an AFM tunnel junction (AFMTJ) based on RuO_2 in which a globally spin-neutral current can be controlled by the orientation of the Néel vector, leading to a tunnel magnetoresistance (TMR) of up to about 500%, which provides an innovative method for detecting the Néel vector of antiferromagnets.[17]

Mn_3X (X = Sn, Ge, Ga, Pt), a hexagonal antiferromagnet with the noncollinear ordering of Mn magnetic moments, exhibits exotic spin transport properties, such as the anomalous Hall effect,[18–20] the anomalous Nernst effect,[21] and the magnetic spin Hall effect.[22] The electrical switching driven by the current-induced spin–orbit torque has achieved in the noncollinear AFM Mn_3Sn, paving the way for future applications in noncollinear spintronics.[23,24] Therefore, it is possible to design AFMTJs with Mn_3X electrodes in which the Néel vector could be controlled by the spin–orbit torque. Based on the density functional theory, a significant TMR as high as 300% has been predicted in the AFMTJ with Mn_3Sn electrodes and a vacuum barrier layer, and a prototype device has been proposed to detect the Néel vector in the noncollinear AFMTJ from a fully electrical way.[25] Very recently, the

Mn_3Pt/MgO/Mn_3Pt AFMTJ has been fabricated experimentally and its TMR under room temperature can reach approximately 100%.[26] According to the theoretical calculations, the TMR effect for the AFMTJ with a MgO insulating layer is found to be largely suppressed compared to that of the vacuum barrier layer.

In order to facilitate scaling of traditional ferromagnetic tunnel junctions to smaller sizes, two-dimensional (2D) materials have been widely used as tunnel barriers, demonstrating exceptional performance such as high TMR ratios, good interface quality, and excellent thermal stability.[27,28] Among the various 2D materials, hexagonal boron nitride (h-BN), a 2D insulator with a large bandgap of ~6 eV, has been proposed as a very promising tunnel barrier candidate for ferromagnetic tunnel junctions both theoretically and experimentally.[29–33] For instance, large-scale monolayer and few-layer h-BN tunnel barriers can be directly grown on a ferromagnetic substrate by the chemical vapor deposition technique, and a TMR of 50% has been obtained for the Co/h-BN/Fe junction.[32] Although the ferromagnetic tunnel junctions with 2D barrier materials have been extensively studied, the effect of 2D tunnel barriers, especially 2D h-BN, on the TMR of AFMTJs is still an open question.

In this Letter, an AFMTJ with noncollinear Mn_3Sn electrodes and a bilayer boron nitride (bi-BN) insulating layer with AA (AA-BN) or AB (AB-BN) stacking is proposed. The TMR effect of the Mn_3Sn/bi-BN/Mn_3Sn noncollinear AFMTJ is investigated using the first-principles calculation in combination with the nonequilibrium Green's function method. The TMR ratios of 97% and 49% are obtained at the Fermi level for the AFMTJs with AA-BN and AB-BN, respectively. The TMR ratio of the Mn_3Sn/AA-BN/Mn_3Sn AFMTJ can be improved to as large as 135% by increasing the chemical potential to 0.1 eV. The enhancement mainly originates from the suppression of the transmission in antiparallel configurations around the K and K' points.

In order to construct an AFMTJ based on noncollinear AFM Mn_3Sn, the bi-BN with AA and AB stacking[34] is adopted as the insulating layer. The structural optimization of Mn_3Sn and bi-BN is performed using the Vienna Ab-initio Simulation Package (VASP) based on the density functional theory.[35,36] A plane wave cutoff energy of 500 eV is used for the calculations and atoms are relaxed with a residual force less than 0.01 eV/Å. The exchange-correlation functional is described using the generalized gradient approximation of Perdew–Burke–Ernzerhof (GGA-PBE).[37] The van der Waals correction of the DFT-D3 method[38] is employed in the structural optimization of bi-BN. The calculated lattice constants of Mn_3Sn, and bi-BN with AA and AB stacking are $a = 5.568$ Å, $a = 2.512$ Å, and $a = 2.545$ Å, respectively. The optimized interlayer distances of bi-BN with AA and AB stacking are 3.65 and 3.44 Å, respectively. Therefore, a 2×2 bi-BN with AA or AB stacking is then sandwiched between two semi-infinite Mn_3Sn electrodes to construct the AFMTJ, as shown in Figs. 1(a) and 1(b). For the Mn_3Sn/bi-BN/Mn_3Sn AFMTJ, it is found that in the most stable configuration, N and B atoms sit atop the nearest and second nearest Mn_3Sn atomic layer, respectively. The optimized distance between Mn_3Sn and bi-BN is 2.1 Å.

The transport properties of Mn_3Sn/bi-BN/Mn_3Sn AFMTJ are calculated using the nonequilibrium Green's function method combined with the density functional theory as implemented in the Nanodcal software.[39] The double-ζ polarized (DZP) atomic orbital linear combination basis is used. The cutoff energy for the real space grid is set to 3000 eV and the convergence criteria for both the density matrix and Hamiltonian are set to 10^{-4} eV. For the self-consistent calculations of electrodes and the two-probe device, $7 \times 7 \times 100$ and $7 \times 7 \times 1$

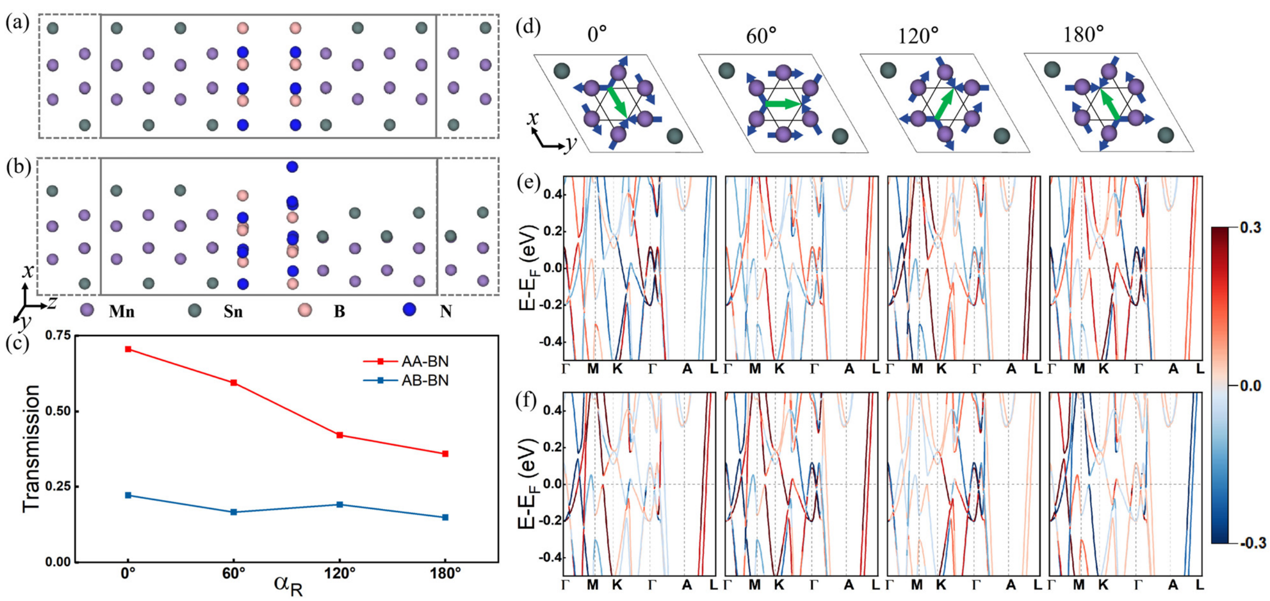

FIG. 1. Schematic of (a) Mn_3Sn/AA-BN/Mn_3Sn AFMTJ and (b) Mn_3Sn/AB-BN/Mn_3Sn AFMTJ. (c) Transmission coefficients for the AFMTJs with AA-BN and AB-BN as a function of Néel vector orientation α_R in the right electrode. (d) The top view of atomic and magnetic structures of AFM Mn_3Sn with the Néel vector orientation of $\alpha = 0°$, 60°, 120°, and 180°. The green arrows indicate the Néel vectors and the blue arrows indicate the spin directions of Mn atoms. The corresponding band structures of Mn_3Sn with the in-plane spin expectation values (e) $\langle\sigma_x\rangle$ and (f) $\langle\sigma_y\rangle$ indicated in color.

k-grids are sampled in the Brillouin zone, respectively. The spin–orbit coupling is considered in the transport calculations. The transmission coefficient of a two-probe system can be expressed as

$$T(E) = \int d\boldsymbol{k}_{\parallel} T(E, \boldsymbol{k}_{\parallel}), \tag{1}$$

where $T(E, \boldsymbol{k}_{\parallel})$ is the $\boldsymbol{k}_{\parallel}$-resolved transmission coefficient which can be given by,[40]

$$T(E, \boldsymbol{k}_{\parallel}) = \mathrm{Tr}\left[\Gamma_L(E, \boldsymbol{k}_{\parallel}) G^r(E, \boldsymbol{k}_{\parallel}) \Gamma_R(E, \boldsymbol{k}_{\parallel}) G^a(E, \boldsymbol{k}_{\parallel})\right]. \tag{2}$$

Here, $G^{r(a)}(E, \boldsymbol{k}_{\parallel})$ is the retarded (advanced) Green's function and $\Gamma_{L(R)}(E, \boldsymbol{k}_{\parallel})$ is the linewidth function describing the coupling between the central region and the left (right) lead at the $\boldsymbol{k}_{\parallel}$ point.

The atomic and magnetic structures of bulk Mn_3Sn are presented in Fig. 1(d). The bulk Mn_3Sn exhibits the hexagonal $D0_{19}$ atomic structure with the $P6_3/mmc$ symmetry.[41] The noncollinear AFM Mn_3Sn is demonstrated to belong to the $Cmc'm'$ magnetic space group and the noncollinear AFM order can be described by the Néel vector orientation α.[25] Figure 1(d) shows four noncollinear AFM states of bulk Mn_3Sn with $\alpha = 0°$, 60°, 120°, and 180°. The calculated band structures with in-plane spin expectation values of bulk Mn_3Sn in four different noncollinear AFM states are shown in Figs. 1(e) and 1(f). It can be found that the spin expectation values gradually change as α changes from 0° to 180°, which is consistent with previous studies.[25] Particularly, the signs of both $\langle\sigma_x\rangle$ and $\langle\sigma_y\rangle$ for each band in Mn_3Sn are opposite at $\alpha = 0°$ and $\alpha = 180°$, which is equivalent to the time-reversal symmetry operation. In our transport calculations, the Néel vector orientation of Mn_3Sn in the left electrode is fixed at $\alpha_L = 0°$ while the Néel vector of the right electrode varies in four different orientations, namely, $\alpha_R = 0°$, 60°, 120°, and 180°. The TMR ratio of the Mn_3Sn/bi-BN/Mn_3Sn AFMTJ is defined as

$$\mathrm{TMR} = \frac{T(\alpha_R = 0°) - T(\alpha_R = 180°)}{T(\alpha_R = 180°)} \times 100\%. \tag{3}$$

We first calculate the transmission coefficients of the Mn_3Sn/bi-BN/Mn_3Sn noncollinear AFMTJ with a fixed $\alpha_L = 0°$ and different α_R. The transmission coefficients for the AFMTJ with AA-BN at the Fermi level are about 0.705, 0.597, 0.422, and 0.360 when the Néel vector is set to be $\alpha_R = 0°$, 60°, 120°, and 180°, respectively, as presented in Fig. 1(c). This indicates that due to the different orientations of the Néel vector in the right electrode, the Mn_3Sn/bi-BN/Mn_3Sn AFMTJ could exhibit four different tunneling resistances, all of which could be utilized in nonvolatile spintronic devices. The TMR ratio of the Mn_3Sn/AA-BN/Mn_3Sn AFMTJ is about 97% with a transmission ratio between the parallel and antiparallel configurations of $\frac{T(\alpha_R=0°)}{T(\alpha_R=180°)} = 1.97$. For the AFMTJ with AB-BN, the transmission coefficients at the Fermi level are about 0.222, 0.166, 0.191, and 0.149 at $\alpha_R = 0°$, 60°, 120°, and 180°, respectively. These values are all less than half of those for the AFMTJ with AA-BN, resulting in a smaller TMR ratio of 49%.

Figures 2(a)–2(d) present the calculated $\boldsymbol{k}_{\parallel}$-resolved transmission coefficients in the 2D Brillouin zone for the Mn_3Sn/AA-BN/Mn_3Sn AFMTJ. For the system with $\alpha_R = 0°$, the spin states in the left and right electrodes are identical. The Mn_3Sn/bi-BN/Mn_3Sn AFMTJ exhibits high transmission coefficients mainly around the Γ point. When the Néel vector of the right electrode is set to $\alpha_R = 60°$, the transmission coefficients around the M point decrease notably compared with

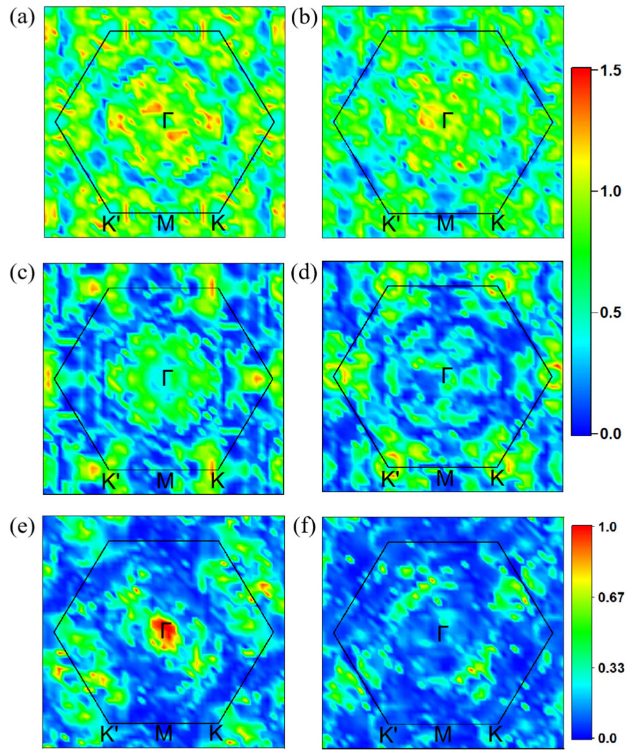

FIG. 2. $\boldsymbol{k}_{\parallel}$-resolved transmission coefficients in the 2D Brillouin zone for the Mn_3Sn/AA-BN/Mn_3Sn AFMTJ with (a) $\alpha_R = 0°$, (b) $\alpha_R = 60°$, (c) $\alpha_R = 120°$, and (d) $\alpha_R = 180°$. $\boldsymbol{k}_{\parallel}$-resolved transmission coefficients in the 2D Brillouin zone for the Mn_3Sn/AB-BN/Mn_3Sn AFMTJ with (e) $\alpha_R = 0°$ and (f) $\alpha_R = 180°$. α_L is fixed to be 0°.

the case of $\alpha_R = 0°$. Specifically, the transmission coefficient at the M point reduces from 0.234 to 0.057 when α_R changes from 0° to 60°. Furthermore, when $\alpha_R = 120°$, it is found that the transmission coefficient near the M point almost vanishes. The transmission coefficient around the Γ point also shows considerable reductions compared with those of $\alpha_R = 0°$ and $\alpha_R = 60°$. In the system with $\alpha_R = 180°$, the spin states of the left and right leads are opposite, resulting in a significant decrease in the transmission coefficients in the entire 2D Brillouin zone due to the wave function mismatch at the interface on the left and right sides. Remarkably, the transmission coefficient at the Γ point reduces from 0.423 in the parallel configuration to 0.242 in the antiparallel configuration.

The $\boldsymbol{k}_{\parallel}$-resolved transmission coefficients in the 2D Brillouin zone for the Mn_3Sn/AB-BN/Mn_3Sn AFMTJ with $\alpha_R = 0°$ and 180° are plotted in Figs. 2(e) and 2(f). It can be found that the transmission coefficient for the system with $\alpha_R = 0°$ mainly originates from the contribution around the Γ point, which significantly decreases when the Néel vector of the right electrode changes to $\alpha_R = 180°$. Moreover, the transmission coefficients almost vanish around the M and K points for both systems with $\alpha_R = 0°$ and $\alpha_R = 180°$, leading to lower tunneling conductances than those for the system with AA-BN.

The TMR of Mn_3Sn/bi-BN/Mn_3Sn AFMTJ at different chemical potentials (μ) is then studied, as presented in Fig. 3(a). For the system with AA-BN, it is found that the TMR increases with the increasing

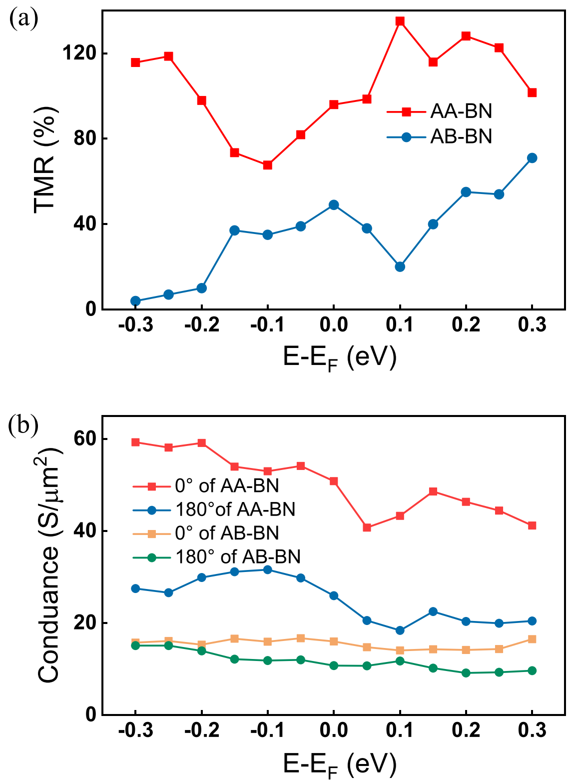

FIG. 3. (a) TMR of the Mn_3Sn/bi-BN/Mn_3Sn AFMTJ as a function of the chemical potential. (b) The tunneling conductance per lateral unit cell area for the AFMTJs with $\alpha = 0°$ and $\alpha = 180°$ as a function of the chemical potential.

chemical potential within the range of μ from -0.1 to 0.1 eV. A significant TMR of 135% occurs at $\mu = 0.1$ eV, which is about 1.4 times that at the Fermi level. Moreover, a notable TMR of 119% is also found at $\mu = -0.25$ eV. The tunneling conductance per lateral unit cell area for systems with $\alpha_R = 0°$ and $\alpha_R = 180°$ are further calculated, as shown in Fig. 3(b). Regardless of the chemical potential, the system in the parallel configuration exhibits higher tunneling conductance compared with that of the antiparallel configuration. When μ ranges from -0.1 to 0.1 eV, the conductance decreases for systems in both parallel and antiparallel configurations as the chemical potential increases. This indicates that the increase in TMR is mainly due to the reduced conductance for the system with $\alpha_R = 180°$. For the AFMTJ with AB-BN, when the chemical potential is negative, the TMR ratio decreases with the decreasing chemical potentials due to the increasing tunneling conductance of the antiparallel configuration. When the chemical potential is positive, the TMR ratio first decreases to its minimum at $\mu = 0.1$ eV. It then rises as the chemical potential increases, which can be attributed to the almost unchanged tunneling conductance of the antiparallel configuration and the increasing conductance of the parallel configurations with the rising chemical potential.

To further understand the maximum TMR of Mn_3Sn/AA-BN/Mn_3Sn AFMTJ at $\mu = 0.1$ eV, the $\boldsymbol{k}_{\parallel}$-resolved transmission coefficients in the 2D Brillouin zone for the parallel and antiparallel configurations are plotted in Fig. 4. From Fig. 4(a), it is found that in the parallel configuration ($\alpha_R = 0°$), the transmission coefficients around

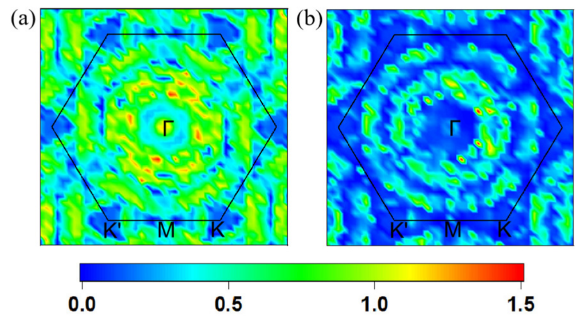

FIG. 4. $\boldsymbol{k}_{\parallel}$-resolved transmission coefficients in the 2D Brillouin zone for the Mn_3Sn/bi-BN/Mn_3Sn AFMTJ in the (a) parallel and (b) antiparallel configurations at $\mu = 0.1$ eV.

K and K' points at $\mu = 0.1$ eV decrease significantly compared with those at the Fermi level as shown in Fig. 2(a), leading to the reduction of total transmission of the Mn_3Sn/AA-BN/Mn_3Sn AFMTJ. While in the antiparallel configuration ($\alpha_R = 180°$), compared with those at the Fermi level shown in Fig. 2(d), the transmission coefficients at $\mu = 0.1$ eV are reduced in most of the 2D Brillouin zone, particularly around the Γ, M, and K points, as depicted in Fig. 4(b). Specifically, the transmission coefficient decreases from 0.331 to 0.105 at the K point when the chemical potential changes from the Fermi level to $\mu = 0.1$ eV.

In order to explain the reduction in transmission coefficient at the K point as μ changes from 0.0 to 0.1 eV for the Mn_3Sn/AA-BN/Mn_3Sn AFMTJ with $\alpha_R = 180°$, the corresponding partial density of states (PDOS) of Mn_3Sn and AA-BN at the at the K point is plotted in Fig. 5(a). Despite the semiconducting behavior of bi-BN, the coupling between Mn_3Sn electrodes and bi-BN induces significant states for AA-BN at the Fermi level, which mainly originates from the p_z orbital of B and N atoms, as well as the p orbital of Mn and Sn atoms. From the charge density difference shown in the inset of Fig. 5(a), notable charge transfer from Mn and Sn atoms to the AA-BN can be found, indicating the strong coupling between the Mn_3Sn and bi-BN. However, the PDOS of Mn_3Sn exhibits a dip at 0.1 eV, leading to very few states for bi-BN. Therefore, the reduction in transmission coefficient at the K point when μ changes from 0.0 to 0.1 eV can be attributed to the electronic structures of Mn_3Sn electrodes. Moreover, the suppression of PDOS for bi-BN can be visualized through the local density of states (LDOS) at the K point in the real space along the transport direction, as shown in Figs. 5(b) and 5(c). It is found that at the Fermi level, the LDOS is mainly contributed by the BN layers and the interfacial Mn atoms. While for the system at $\mu = 0.1$ eV, the LDOS at the interface of Mn_3Sn/AA-BN/Mn_3Sn AFMTJ, particularly the LDOS on the BN layers, is severely depressed, which hinders the electron transport through the bilayer BN. As a result, the transmission coefficient at the K point is greatly suppressed, leading to the remarkably high TMR for the Mn_3Sn/AA-BN/Mn_3Sn AFMTJ at $\mu = 0.1$ eV. In practical applications, the chemical potential could be adjusted through doping or gate voltage, providing the potential to enhance the TMR of AFMTJ devices.

Our proposed AFMTJs with a 2D insulating layer could have practical applications, similar to the all-AFMTJs based on Mn_3Sn and Mn_3Pt noncollinear antiferromagnets with nonmagnetic metal oxide insulator.[26,42,43] In these experimental work, antiferromagnets were epitaxially grown on the metal oxide substrates and the AFM order

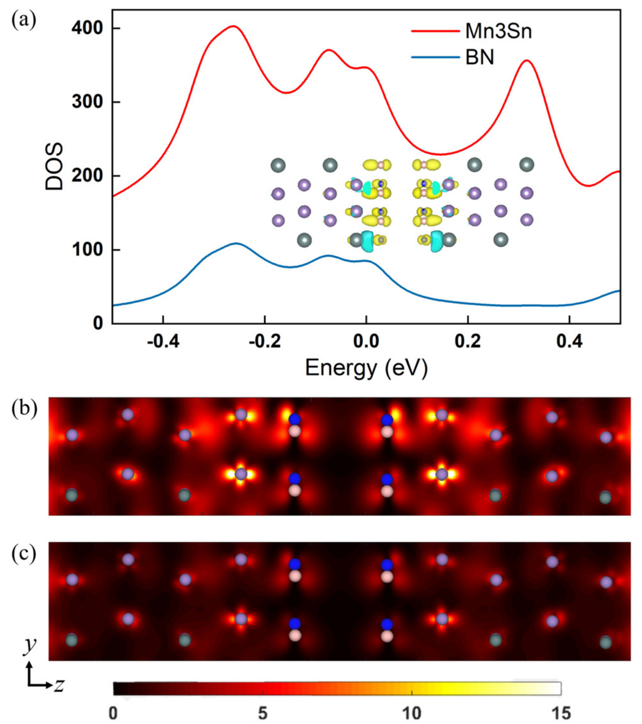

FIG. 5. (a) Partial density of states (PDOS) of Mn_3Sn and AA-BN at the *K* point for the Mn_3Sn/AA-BN/Mn_3Sn AFMTJ in the antiparallel configuration. Inset: charge density difference of the scattering region. Local density of states at the *K* point in the real space along the transport direction for the Mn_3Sn/AA-BN/Mn_3Sn AFMTJ in the antiparallel configuration at (b) $\mu = 0$ and (c) $\mu = 0.1$ eV.

was manipulated by external magnetic fields or current-induced spin–orbit torque. A room-temperature TMR ratio of around 2% is achieved for the Mn_3Sn/MgO/Mn_3Sn AFMTJ, while the TMR ratios for Mn_3Pt/MgO/Mn_3Pt and Mn_3Pt/Al_2O_3/Mn_3Pt AFMTJs are about 100% and 110%, respectively. In addition, the antiferromagnetic Mn_3Sn is separated by the Ag layer, rather than the insulating barrier, and reaches a maximum magnetoresistance of 0.3% at 300 K.[44] Our calculated TMR ratio for Mn3Sn-based AFMTJs with a 2D insulating barrier is much higher than the experimental data of the Mn_3Sn/MgO/Mn_3Sn AFMTJ, which suggests that using 2D materials as insulating layers could greatly improve the TMR ratio of Mn_3X-based noncollinear AFMTJs. However, it should be noted that our simulation only consider ballistic transport, leading to an overestimation of the AFMTJ performance.

It is also worth noting that, in addition to nonmagnetic 2D materials, using 2D ferromagnetic materials as tunnel barriers in ferromagnetic tunnel junctions has shown inspiring prospects in achieving high TMR ratios.[45–47] Very recently, ultrahigh TMR ratios and high spin injection efficiency have been predicted in magnetic tunnel junctions based on ferromagnetic Weyl half-metals.[47] Therefore, it is expected that significant improvements in the performance of AFMTJs could be realized by utilizing 2D antiferromagnetic half-metals with electrically controllable antiferromagnetic states.

In summary, we have proposed a Mn_3Sn-based noncollinear AFMTJ with a bilayer BN insulating layer and investigated its TMR ratio by using the first-principles method combined with the nonequilibrium Green's function. It is found that four different tunneling resistance states can be achieved due to varied orientations of the Néel vector in electrodes. The TMR ratios of 97% and 49% are obtained in the AFMTJs with AA-BN and AB-BN as the insulating layers. Moreover, the TMR ratio could be increased by adjusting the chemical potentials, reaching about 135% at $\mu = 0.1$ eV for the Mn_3Sn/AA-BN/Mn_3Sn AFMTJ. This enhancement is mainly due to the reduction in the transmission of antiparallel configurations around the *K* and *K'* points. Our results demonstrate promising ways for detecting the Néel vector in noncollinear AFM materials using the TMR effect proposed by Shao *et al.*,[17] and further suggest possible applications of noncollinear AFMTJs with 2D tunnel barriers in future spintronics.

This work was financially supported by the National Natural Science Foundation of China (Grant Nos. 12074190 and 12074230), the Fund for Shanxi "1331 Project," and the Shanxi Scholarship Council of China.

AUTHOR DECLARATIONS

Conflict of Interest

The authors have no conflicts to disclose.

Author Contributions

Zhanran Wang: Investigation (lead); Visualization (lead); Writing – original draft (lead). **Bo Bian:** Investigation (supporting); Visualization (supporting). **Lei Zhang:** Supervision (equal); Writing – review & editing (equal). **Zhizhou Yu:** Supervision (equal); Writing – review & editing (equal).

DATA AVAILABILITY

The data that support the findings of this study are available from the corresponding author upon reasonable request.

REFERENCES

1. T. Jungwirth, X. Marti, P. Wadley, and J. Wunderlich, "Antiferromagnetic spintronics," Nat. Nanotechnol. **11**, 231–241 (2016).
2. T. Jungwirth, J. Sinova, A. Manchon, X. Marti, J. Wunderlich, and C. Felser, "The multiple directions of antiferromagnetic spintronics," Nat. Phys. **14**, 200–203 (2018).
3. V. Baltz, A. Manchon, M. Tsoi, T. Moriyama, T. Ono, and Y. Tserkovnyak, "Antiferromagnetic spintronics," Rev. Mod. Phys. **90**, 015005 (2018).
4. L. Šmejkal, Y. Mokrousov, B. Yan, and A. H. MacDonald, "Topological antiferromagnetic spintronics," Nat. Phys. **14**, 242–251 (2018).
5. J. Železný, P. Wadley, K. Olejník, A. Hoffmann, and H. Ohno, "Spin transport and spin torque in antiferromagnetic devices," Nat. Phys. **14**, 220–228 (2018).
6. J. Han, R. Cheng, L. Liu, H. Ohno, and S. Fukami, "Coherent antiferromagnetic spintronics," Nat. Mater. **22**, 684–695 (2023).
7. H. Yan, X. Zhou, P. Qin, and Z. Liu, "Review on spin-split antiferromagnetic spintronics," Appl. Phys. Lett. **124**, 030503 (2024).
8. P. Wadley, B. Howells, J. Železnỳ, C. Andrews, V. Hills, R. P. Campion, V. Novák, K. Olejník, F. Maccherozzi, S. Dhesi *et al.*, "Electrical switching of an antiferromagnet," Science **351**, 587–590 (2016).
9. K. Olejník, T. Seifert, Z. Kašpar, V. Novák, P. Wadley, R. P. Campion, M. Baumgartner, P. Gambardella, P. Němec, J. Wunderlich *et al.*, "Terahertz electrical writing speed in an antiferromagnetic memory," Sci. Adv. **4**, eaar3566 (2018).
10. X. Chen, R. Zarzuela, J. Zhang, C. Song, X. Zhou, G. Shi, F. Li, H. Zhou, W. Jiang, F. Pan *et al.*, "Antidamping-torque-induced switching in biaxial antiferromagnetic insulators," Phys. Rev. Lett. **120**, 207204 (2018).

[11] X. Chen, X. Zhou, R. Cheng, C. Song, J. Zhang, Y. Wu, Y. Ba, H. Li, Y. Sun, Y. You *et al.*, "Electric field control of Néel spin–orbit torque in an antiferromagnet," Nat. Mater. **18**, 931–935 (2019).
[12] S. Y. Bodnar, L. Šmejkal, I. Turek, T. Jungwirth, O. Gomonay, J. Sinova, A. Sapozhnik, H.-J. Elmers, M. Kläui, and M. Jourdan, "Writing and reading antiferromagnetic Mn_2Au by Néel spin-orbit torques and large anisotropic magnetoresistance," Nat. Commun. **9**, 348 (2018).
[13] G. R. Hoogeboom, A. Aqeel, T. Kuschel, T. T. M. Palstra, and B. J. van Wees, "Negative spin Hall magnetoresistance of Pt on the bulk easy-plane antiferromagnet NiO," Appl. Phys. Lett. **111**, 052409 (2017).
[14] J. Fischer, O. Gomonay, R. Schlitz, K. Ganzhorn, N. Vlietstra, M. Althammer, H. Huebl, M. Opel, R. Gross, S. T. Goennenwein *et al.*, "Spin hall magnetoresistance in antiferromagnet/heavy-metal heterostructures," Phys. Rev. B **97**, 014417 (2018).
[15] L. Baldrati, A. Ross, T. Niizeki, C. Schneider, R. Ramos, J. Cramer, O. Gomonay, M. Filianina, T. Savchenko, D. Heinze *et al.*, "Full angular dependence of the spin hall and ordinary magnetoresistance in epitaxial antiferromagnetic NiO (001)/Pt thin films," Phys. Rev. B **98**, 024422 (2018).
[16] C. Chiang, S. Huang, D. Qu, P. Wu, and C. Chien, "Absence of evidence of electrical switching of the antiferromagnetic Néel vector," Phys. Rev. Lett. **123**, 227203 (2019).
[17] D.-F. Shao, S.-H. Zhang, M. Li, C.-B. Eom, and E. Y. Tsymbal, "Spin-neutral currents for spintronics," Nat. Commun. **12**, 7061 (2021).
[18] S. Nakatsuji, N. Kiyohara, and T. Higo, "Large anomalous hall effect in a non-collinear antiferromagnet at room temperature," Nature **527**, 212–215 (2015).
[19] X. Li, L. Xu, L. Ding, J. Wang, M. Shen, X. Lu, Z. Zhu, and K. Behnia, "Anomalous Nernst and Righi-Leduc effects in Mn_3Sn: Berry curvature and entropy flow," Phys. Rev. Lett. **119**, 056601 (2017).
[20] Z. H. Liu, Y. J. Zhang, G. D. Liu, B. Ding, E. K. Liu, H. M. Jafri, Z. P. Hou, W. H. Wang, X. Q. Ma, and G. H. Wu, "Transition from anomalous hall effect to topological hall effect in hexagonal non-collinear magnet Mn_3Ga," Sci. Rep. **7**, 515 (2017).
[21] M. Ikhlas, T. Tomita, T. Koretsune, M.-T. Suzuki, D. Nishio-Hamane, R. Arita, Y. Otani, and S. Nakatsuji, "Large anomalous Nernst effect at room temperature in a chiral antiferromagnet," Nat. Phys. **13**, 1085–1090 (2017).
[22] M. Kimata, H. Chen, K. Kondou, S. Sugimoto, P. K. Muduli, M. Ikhlas, Y. Omori, T. Tomita, A. H. MacDonald, S. Nakatsuji, and Y. Otani, "Magnetic and magnetic inverse spin hall effects in a non-collinear antiferromagnet," Nature **565**, 627–630 (2019).
[23] H. Tsai, T. Higo, K. Kondou, T. Nomoto, A. Sakai, A. Kobayashi, T. Nakano, K. Yakushiji, R. Arita, S. Miwa, Y. Otani, and S. Nakatsuji, "Electrical manipulation of a topological antiferromagnetic state," Nature **580**, 608–613 (2020).
[24] Y. Takeuchi, Y. Yamane, J.-Y. Yoon, R. Itoh, B. Jinnai, S. Kanai, J. Ieda, S. Fukami, and H. Ohno, "Chiral-spin rotation of non-collinear antiferromagnet by spin–orbit torque," Nat. Mater. **20**, 1364–1370 (2021).
[25] J. Dong, X. Li, G. Gurung, M. Zhu, P. Zhang, F. Zheng, E. Y. Tsymbal, and J. Zhang, "Tunneling magnetoresistance in noncollinear antiferromagnetic tunnel junctions," Phys. Rev. Lett. **128**, 197201 (2022).
[26] P. Qin, H. Yan, X. Wang, H. Chen, Z. Meng, J. Dong, M. Zhu, J. Cai, Z. Feng, X. Zhou *et al.*, "Room-temperature magnetoresistance in an all-antiferromagnetic tunnel junction," Nature **613**, 485–489 (2023).
[27] E. Elahi, G. Dastgeer, P. R. Sharma, S. Nisar, M. Suleman, M. W. Iqbal, M. Imran, M. Aslam, and A. Imran, "A brief review on the spin valve magnetic tunnel junction composed of 2D materials," J. Phys. D **55**, 423001 (2022).
[28] J.-F. Dayen, S. J. Ray, O. Karis, I. J. Vera-Marun, and M. V. Kamalakar, "Two-dimensional van der Waals spinterfaces and magnetic-interfaces," Appl. Phys. Rev. **7**, 011303 (2020).
[29] V. M. Karpan, P. A. Khomyakov, G. Giovannetti, A. A. Starikov, and P. J. Kelly, "Ni(111)|graphene|h-BN junctions as ideal spin injectors," Phys. Rev. B **84**, 153406 (2011).
[30] M. L. Hu, Z. Yu, K. W. Zhang, L. Z. Sun, and J. X. Zhong, "Tunneling magnetoresistance of bilayer hexagonal boron nitride and its linear response to external uniaxial strain," J. Phys. Chem. C **115**, 8260–8264 (2011).
[31] M. Piquemal-Banci, R. Galceran, S. Caneva, M.-B. Martin, R. S. Weatherup, P. R. Kidambi, K. Bouzehouane, S. Xavier, A. Anane, F. Petroff, A. Fert, J. Robertson, S. Hofmann, B. Dlubak, and P. Seneor, "Magnetic tunnel junctions with monolayer hexagonal boron nitride tunnel barriers," Appl. Phys. Lett. **108**, 102404 (2016).
[32] M. Piquemal-Banci, R. Galceran, F. Godel, S. Caneva, M.-B. Martin, R. S. Weatherup, P. R. Kidambi, K. Bouzehouane, S. Xavier, A. Anane, F. Petroff, A. Fert, S. M.-M. Dubois, J.-C. Charlier, J. Robertson, S. Hofmann, B. Dlubak, and P. Seneor, "Insulator-to-metallic spin-filtering in 2D-magnetic tunnel junctions based on hexagonal boron nitride," ACS Nano **12**, 4712–4718 (2018).
[33] H. Lu, Y. Guo, and J. Robertson, "*Ab initio* study of hexagonal boron nitride as the tunnel barrier in magnetic tunnel junctions," ACS Appl. Mater. Interfaces **13**, 47226–47235 (2021).
[34] S. M. Gilbert, T. Pham, M. Dogan, S. Oh, B. Shevitski, G. Schumm, S. Liu, P. Ercius, S. Aloni, M. L. Cohen, and A. Zettl, "Alternative stacking sequences in hexagonal boron nitride," 2D Mater. **6**, 021006 (2019).
[35] G. Kresse and J. Furthmüller, "Efficient iterative schemes for *ab initio* total-energy calculations using a plane-wave basis set," Phys. Rev. B **54**, 11169–11186 (1996).
[36] G. Kresse and D. Joubert, "From ultrasoft pseudopotentials to the projector augmented-wave method," Phys. Rev. B **59**, 1758–1775 (1999).
[37] J. P. Perdew, K. Burke, and M. Ernzerhof, "Generalized gradient approximation made simple," Phys. Rev. Lett. **77**, 3865–3868 (1996).
[38] S. Grimme, J. Antony, S. Ehrlich, and H. Krieg, "A consistent and accurate ab initio parametrization of density functional dispersion correction (DFT-D) for the 94 elements H-Pu," J. Chem. Phys. **132**, 154104 (2010).
[39] J. Taylor, H. Guo, and J. Wang, "*Ab initio* modeling of quantum transport properties of molecular electronic devices," Phys. Rev. B **63**, 245407 (2001).
[40] D. Waldron, V. Timoshevskii, Y. Hu, K. Xia, and H. Guo, "First principles modeling of tunnel magnetoresistance of Fe/MgO/Fe trilayers," Phys. Rev. Lett. **97**, 226802 (2006).
[41] P. J. Brown, V. Nunez, F. Tasset, J. B. Forsyth, and P. Radhakrishna, "Determination of the magnetic structure of Mn_3Sn using generalized neutron polarization analysis," J. Phys.: Condens. Matter **2**, 9409 (1990).
[42] X. Chen, T. Higo, K. Tanaka, T. Nomoto, H. Tsai, H. Idzuchi, M. Shiga, S. Sakamoto, R. Ando, H. Kosaki, T. Matsuo, D. Nishio-Hamane, R. Arita, S. Miwa, and S. Nakatsuji, "Octupole-driven magnetoresistance in an antiferromagnetic tunnel junction," Nature **613**, 490–495 (2023).
[43] J. Shi, S. Arpaci, V. Lopez-Dominguez, V. K. Sangwan, F. Mahfouzi, J. Kim, J. G. Athas, M. Hamdi, C. Aygen, H. Arava, C. Phatak, M. Carpentieri, J. S. Jiang, M. A. Grayson, N. Kioussis, G. Finocchio, M. C. Hersam, and P. Khalili Amiri, "Electrically controlled all-antiferromagnetic tunnel junctions on silicon with large room-temperature magnetoresistance," Adv. Mater. **36**, e2312008 (2024).
[44] X. Wang, H. Chen, H. Yan, P. Qin, X. Zhou, Z. Meng, L. Liu, X. Liu, H. Wang, and Z. Liu, "Room-temperature magnetoresistance in a single-layer composite film based on noncollinear antiferromagnetic Mn_3Sn," Appl. Phys. Lett. **122**, 152403 (2023).
[45] Z. Yan, R. Zhang, X. Dong, S. Qi, and X. Xu, "Significant tunneling magnetoresistance and excellent spin filtering effect in CrI_3-based van der waals magnetic tunnel junctions," Phys. Chem. Chem. Phys. **22**, 14773–14780 (2020).
[46] F. Li, B. Yang, Y. Zhu, X. Han, and Y. Yan, "Ultrahigh tunneling magnetoresistance in van der Waals and lateral magnetic tunnel junctions formed by intrinsic ferromagnets $Li_{0.5}CrI_3$ and CrI_3," Appl. Phys. Lett. **117**, 022412 (2020).
[47] J. Tan, G. Yang, and G. Ouyang, "Large tunneling magnetoresistance and its high bias stability in Weyl half-semimetal based lateral magnetic tunnel junctions," New J. Phys. **26**, 033047 (2024).